Wake Aerodynamic of Multi-Rotor System with Lifting-Devices under Different Ambient Turbulence

Li, Yuantso; Yu, Wei; Sciacchitano, Andrea; Ferreira, Carlos

DOI
10.1088/1742-6596/3016/1/012042

Publication date
2025

Document Version
Final published version

Published in
Journal of Physics: Conference Series

Journal of Physics:
Conference Series

PAPER • OPEN ACCESS

Wake Aerodynamic of Multi-Rotor System with Lifting-Devices Under Different Ambient Turbulence

To cite this article: YuanTso Li *et al* 2025 *J. Phys.: Conf. Ser.* **3016** 012042

Journal of Physics: Conference Series **3016** (2025) 012042 doi:10.1088/1742-6596/3016/1/012042

Wake Aerodynamic of Multi-Rotor System with Lifting-Devices Under Different Ambient Turbulence

YuanTso Li[1], Wei Yu[1], Andrea Sciacchitano[1], and Carlos Ferreira[1]

[1] Faculty of Aerospace Engineering, Delft University of Technology, Delft, the Netherlands

E-mail: `Y.Li-18@tudelft.nl`

Abstract. The aerodynamics of the multi-rotor system with lifting-devices (MRSL), an innovative concept of wind energy harvesting machine, is preliminary investigated using Large Eddy Simulation (LES) with actuator techniques. In the current setup, turbulent inflow conditions are considered, but inflow wind shear is excluded. Consistent with previous studies, the results demonstrate faster wake recovery of the MRSL compared to its conventional counterpart, namely the wind turbine system without the lifting-devices. Additionally, a set of high-fidelity simulations further reveals that the enhanced wake recovery is robust under both laminar and turbulent inflow conditions, remaining largely unaffected by variations in the ambient turbulence level. The present work provides proof-of-concept evidence that the effectiveness of MRSLs is not significantly hindered by ambient turbulence, motivating future research to evaluate their performance within a realistic atmospheric boundary layer.

1. Introduction

The intensive land use of wind energy is one of its key disadvantages. The median electricity generation rate per unit area for wind energy is 2.8 W/m^2, substantially lower than that of solar photovoltaic (PV), which is 8.4 W/m^2 [1]. This limitation hinders wind energy development, as suitable sites are scarce and often compete with other essential land uses, such as agriculture, maritime shipping, and ecological reserves [2].

The low vertical energy entrainment rate is a key factor that leads to the intensive land use of wind energy, as it slows wake recovery within wind farms and reduces the power generation efficiency of turbines under waked conditions [3]. To address this limitation, Ferreira [4] proposed an innovative wind energy harvesting system, namely the Multi-Rotor System with Lifting-devices (MRSL), illustrated in Figure 1. The concept of MRSL leverages strong vertical flow induced by the tip-vortices of its lifting-devices. Recent studies have shown that the wake of MRSL experiences much faster recovery than its conventional counterpart, as demonstrated through both experimental [5] and numerical investigations [6]. Furthermore, when immersed in atmospheric boundary layers, computational fluid dynamics (CFD) simulations of Li *et al.* [7] indicate that clustered MRSLs, termed *regenerative wind farms* (RGWFs) [4], can harvest twice the wind power of conventional counterparts using the same land area due to the enhanced energy entrainment. These promising results highlight the potential of MRSLs and RGWFs as transformative technologies/concepts that can address the challenges in meeting the climate targets set by the Paris Agreement [8], which are currently at risk of being missed [2, 9, 10].

This study further investigates the wake aerodynamics of isolated MRSL using a high-fidelity CFD model, which is large-eddy simulation (LES) with actuator techniques. Unlike the RANS

Journal of Physics: Conference Series **3016** (2025) 012042 doi:10.1088/1742-6596/3016/1/012042

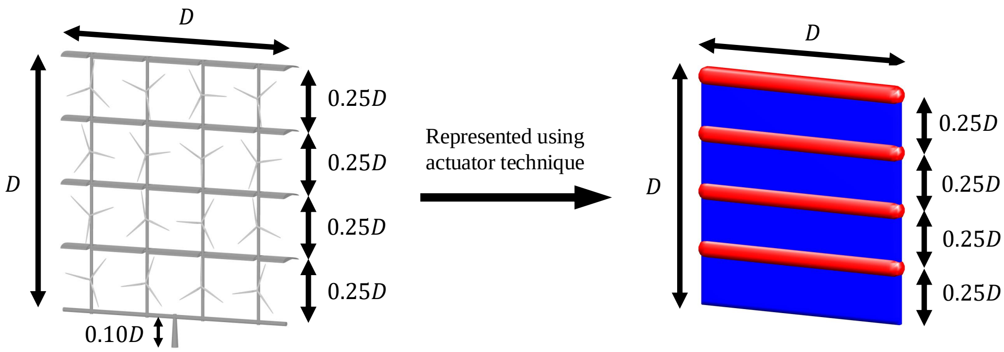

Figure 1. Left: A sketch illustrating how the multi-rotor system with lifting-devices (MRSL) could be in the real world. With the orientation of the wings, this MRSL is in **Down-Washing** configuration [7]. Right: MRSL represented with the actuator techniques. The rotor parts are parametrized as an actuator disk (blue surface). The lifting-devices/wings are degenerated into actuator lines (red surfaces). The key dimensions are labeled on both sides, with D being 300 m.

(Reynolds-averaged Navier–Stokes) approaches used in the previous works [6, 7], LES provides detailed time-resolved data, enabling the close examination of transient phenomena. This study focuses on the effects of inflow turbulence intensity (TI_∞) on MRSL's wake structures and the underlying mechanisms of wake recovery. On the other hand, wind shear are intentionally excluded to better isolate the impacts of TI_∞. Additionally, animations of the time-varying flow fields and the CFD simulation settings are available in the accompanying data repository [11]. Through this work, enhanced understanding of MRSL's wake aerodynamics is given and offers insights for upcoming research and future designs.

2. Descriptions of MRSL

The innovative wind energy harvesting system, the multi-rotor system with lifting-devices (MRSL), is conceptualized in Figure 1. The conceptualized MRSL consists of several wind turbines as the sub-rotors and four wings. Based on the orientation of the wings, the MRSL's configurations are classified as **Up-Washing** (**UW**), **Down-Washing** (**DW**), and **Without-Lifting** (**WL**). The lifting-devices in configurations **UW** and **DW** channel the MRSL's wake upward and downward, respectively. Configuration **WL** does not have the lifting-devices and serves as the reference representing the conventional wind energy harvesting machines.

The dimensions of MRSL used in this study are shown in Figure 1. MRSL's frontal area is modeled as a square with a side length D of 300 m and a clearance to ground of 30 m ($0.10D$). It includes four straight wings, each with a span of D and a chord of 37.5 m ($D/8$). The wings are positioned at 25%, 50%, 75%, and 100% of the MRSL's height. The thrust coefficient C_T of the rotor is targeted to 0.7, and the wing's airfoil polar is based on S1223 airfoil [12].

To avoid exceptionally high computational costs, the complex geometry of MRSL is simplified using actuator techniques [13, 14], as abstractly illustrated in the right panel of Figure 1. Further details on the parametrization of the MRSL are provided in the following section.

3. Methodology

3.1. Modeling MRSL

As mentioned in the previous section, the MRSL is parametrized using actuator techniques in the CFD simulations. This is achieved through implementing `flyingActuationDiskSource`, a customized OpenFOAM module that has been developed in the the work of Li *et al.* [7]. Most

Journal of Physics: Conference Series **3016** (2025) 012042 doi:10.1088/1742-6596/3016/1/012042

parameters used in this study are consistent with those in that work. This subsection highlights only the key parameters and those that are modified. For additional details, referred to Li *et al.* [7] and the case settings provided in the accompanied data repository [11].

The rotor components of the MRSL are modeled using 30×30 equally-spaced actuator elements as a whole. The element spacing Δ^{ele} is $D/30$ and the geometries of the sub-rotors is largely simplified. C_T of the surface is targeted at 0.7 (see Section 3 of Li *et al.* [7] for details). A Gaussian regularization kernel is employed to project the actuator element forces onto the CFD grid as body force fields. Unlike the classic isotropic kernel [13], this study utilizes a non-isotropic kernel [15], described in Equation 1, where $\boldsymbol{d}$ is the vector from the actuator element to the target grid point. For the rotor, smearing factors are set as $\varepsilon_x^R = 2\varepsilon_y^R = 2\varepsilon_z^R = 2\Delta^{\mathrm{ele}}$ (see Figure 2 for the definition of the coordinate, superscript R indicates "Rotor"). These values balance reducing the numerical singularity and keeping the force concentrated [16].

$$\eta_\varepsilon\big(\boldsymbol{d} = (d_x, d_y, d_z)\big) = \frac{1}{\pi^{3/2}\varepsilon_x\varepsilon_y\varepsilon_z}\exp\left\{\left(-\frac{d_x^2}{\varepsilon_x^2} - \frac{d_y^2}{\varepsilon_y^2} - \frac{d_z^2}{\varepsilon_z^2}\right)\right\} \tag{1}$$

The lifting-devices/wings of MRSL are modeled as four actuator lines, each consisting of 30 equally-spaced actuator elements with a spacing of $D/30$. Similar to Li *et al.* [7], the wings have a constant chord along the span and have no twist. The polar data for the wings is based on S1223 airfoil [12]. The pitch angle θ_p of the wings is dynamically adjusted during simulations to align the angle of attack at the mid-span, α_{mid}, with the target value $\alpha_{\mathrm{mid}}^{\mathrm{Target}} = 8.5°$. This $\alpha_{\mathrm{mid}}^{\mathrm{Target}}$ corresponds to a mid-span lift coefficient $C_{l,\mathrm{mid}} = 2.2$. To avoid pitching the wings over frequently or pitching them too rapidly, a one-sided exponential time filter with a 30 s window is applied to the measured discrepancy between α_{mid} and $\alpha_{\mathrm{mid}}^{\mathrm{Target}}$ and the maximum pitching rate is limited to $0.5°\ \mathrm{s}^{-1}$.

See Li *et al.* [7] for further descriptions on modeling MRSL with actuator techniques, including velocity sampling, force calculation and projection, and the wings' smearing factors (ε^W).

3.2. Numerical setups

This work employs LES approach, using *OpenFOAM v2312* [17] as the software. The flow is treated as incompressible and Newtonian ($\rho = 1.225$ kg/m^3, $\nu = 1.5 \times 10^{-5}$ m^2/s) with thermal effects neglected. The sub-grid scale (SGS) effects are modeled using the dynamic Smagorinsky model with Lagrangian averaging (`dynamicLagrangian`) [18]. Turbulent inflow is generated using a synthetic method, DFSEM (divergence-free synthetic eddy method, `turbulentDFSEMInlet`) [19]. DFSEM had been successfully implemented for similar wind energy applications [20, 21]. The mean inflow velocity is $(u_\infty, v_\infty, w_\infty) = (10.1, 0.0, 0.0)$ m/s, with a range of inflow turbulence intensity TI_∞ as shown in Table 1. Note that wind shear is excluded.

The computational domain spans $21.5D \times 5.0D \times 5.0D$ in streamwise (x), lateral (y), and vertical (z) directions. The MRSL's streamwise position is defined as $x/D = 0$, which is $8D$ away from the inlet. The mesh is first constructed with cubic cells of size $D/30$ (matching Δ^{ele}), and then undergoes two refinements. The first is around the ground, where the bottom layer is further divided into 8 layers in the vertical direction with an expansion ratio of 1.1. The second is near the inlet and is only implemented for the cases subjected to turbulent inflows, where the cell dimensions are halved in all directions for the first $0.5D$ to mitigate pressure fluctuations caused by DFSEM [20]. The mesh comprises 17.8M cells. The ground, sides, and top of the domain are treated as slip walls. The Courant–Friedrichs–Lewy number is set to around 0.05, and PISO (Pressure-Implicit with Splitting of Operators) algorithm is implemented. Statistical data is collected between $60.6 \leq \tilde{t} \leq 121.2$ ($\tilde{t} = tu_\infty/D$), excluding the initialization phase.

Further descriptions of the simulation setup, including boundary conditions and discretization schemes, are available in the accompanying data repository [11].

4. Test metrics

The case numbers and setups for the simulation cases are listed in Table 1. To avoid repetition, the results of the MRSL performance, such as the normalized-time-averaged forces exerted and power harvested, are concatenated and will be elaborated in Section 5.1. In these cases, the configuration of MRSL is categorized based on how its lifting-devices manipulate the wake, as described in Section 2. In Table 1, each configuration is tested with several different TI_∞, including laminar inflow conditions. The integral timescale, Λ_∞, is defined as $\Lambda_\infty = \int_0^{\tau_0} R_{uu}(\tau)\,\mathrm{d}\tau$, where R_{uu} is the time correlation function of u and τ_0 is the first τ for which $R_{uu}(\tau)$ crosses zero. All the turbulence spectra are Kolmogorov-like (not shown, similar to those in Figure 3 of Li *et al.* [20]), and both TI_∞ and Λ_∞ are sampled at $x/D = -2.0$.

In the following, the results of cases subjected to $\mathrm{TI}_\infty = 5.37\%$ are emphasized, as this TI_∞ falls within the typical range for offshore environments (5–8%) [22]. Cases with TI_∞ higher than 5.37% are not tested due to the convergence issues associated with the turbulence model used.

Table 1. Test matrix of the simulation cases tested. The four leftmost columns are the case number, the tested MRSL's configuration, the tested inflow turbulence intensity (TI_∞), and the corresponding integral timescale (Λ_∞). The results of MRSL's performance are appended on the right. $\overline{C}_T$ and $\overline{C}_P$ are the time-averaged thrust and power coefficients, defined in Equation 2. $\widehat{T}^R$, $\widehat{L}^W$, $\widehat{D}^W$, and $\widehat{P}^R$ are the normalized-time-averaged rotor's thrust, wings' lift, wings' drag, and rotor's power, respectively, and their definitions are in Equation 3. The normalization factors are based on the thrust and power of case **WL-53**.

Case number	MRSL's configuration	TI_∞	$\Lambda_\infty u_\infty/D$	$\overline{C}_T$	$\overline{C}_P$	$\widehat{T}^R$	$\widehat{L}^W$	$\widehat{D}^W$	$\widehat{P}^R$
UW-00	**Up-Washing**	Laminar	–	0.77	0.64	108%	99%	17%	113%
UW-17		1.72%	0.24	0.77	0.64	109%	101%	18%	114%
UW-36		3.69%	0.22	0.77	0.64	109%	101%	18%	114%
UW-53		5.37%	0.25	0.77	0.64	108%	100%	18%	114%
WL-00	**Without-Lifting**	Laminar	–	0.71	0.56	100%	–	–	100%
WL-17		1.72%	0.24	0.71	0.56	100%	–	–	100%
WL-36		3.69%	0.22	0.71	0.56	100%	–	–	100%
WL-53		**5.37%**	**0.25**	**0.70**	**0.56**	**100%**	**–**	**–**	**100%**
DW-00	**Down-Washing**	Laminar	–	0.63	0.48	89%	103%	5%	86%
DW-17		1.72%	0.24	0.63	0.48	89%	102%	5%	86%
DW-36		3.69%	0.22	0.63	0.48	89%	101%	5%	86%
DW-53		5.37%	0.25	0.63	0.48	89%	101%	5%	86%

5. Results and Discussion

5.1. Performance of MRSL

In this work, T^R, L^W, D^W, and P^R are the rotor's thrust, wings' lift, wings' drag, and rotor's power, respectively. Sampling methods of these quantities are detailed in Li *et al.* [7]. C_T and C_P are the rotor's thrust and power coefficients, and their definition is in Equation 2. Operators overline ($\overline{\cdot}$) and hat ($\widehat{\cdot}$) denote time-averaging and time-averaged-normalizing, respectively. The normalization is performed by dividing the forces or power against the thrust ($\overline{T}^R_{\textbf{WL-53}}$) or power ($\overline{P}^R_{\textbf{WL-53}}$) of the reference case **WL-53**, as written in Equation 3.

$$\overline{C}_T \triangleq \frac{\overline{T}^R}{0.5\rho u_\infty^2 D^2}, \qquad \overline{C}_P \triangleq \frac{\overline{P}^R}{0.5\rho u_\infty^3 D^2} \tag{2}$$

$$\widehat{T}^R \triangleq \frac{\overline{T}^R}{\overline{T}^R_{\textbf{WL-53}}}, \qquad \widehat{L}^W \triangleq \frac{\left|\overline{L}^W\right|}{\overline{T}^R_{\textbf{WL-53}}}, \qquad \widehat{D}^W \triangleq \frac{\overline{D}^W}{\overline{T}^R_{\textbf{WL-53}}}, \qquad \widehat{P}^R \triangleq \frac{\overline{P}^R}{\overline{P}^R_{\textbf{WL-53}}} \tag{3}$$

Journal of Physics: Conference Series **3016** (2025) 012042 doi:10.1088/1742-6596/3016/1/012042

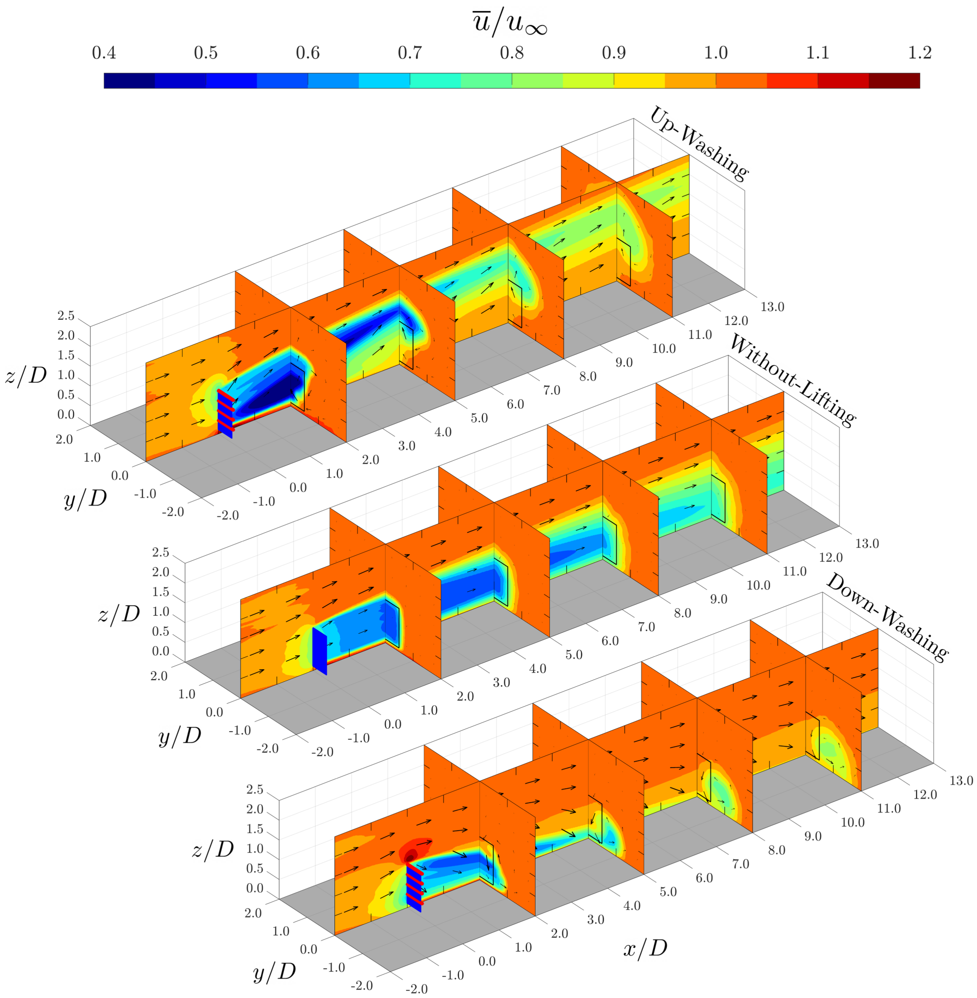

Figure 2. Contours of time-averaged streamwise velocity ($\overline{u}$) for cases **UW-53** (top), **WL-53** (middle), and **DW-53** (bottom). Arrows are scaled by the square root of the in-plane velocity norm. The rotor part and lifting-devices of MRSL are represented by blue and red surfaces, respectively. The MRSL projection areas are outlined as squares in each x-plane.

$\overline{C}_T$, $\overline{C}_P$, $\widehat{T}^R$, $\widehat{L}^W$, $\widehat{D}^W$, and $\widehat{P}^R$ are summarized on the right of Table 1. As designed, magnitudes of $\widehat{L}^W$ are comparable to $\widehat{T}^R$ for cases with configurations **UW** and **DW**. Moreover, the performance of MRSL is insensitive to TI_∞. On the other hand, MRSL's configuration significantly influences its performance. Specifically, $\widehat{T}^R$ and $\widehat{P}^R$ for cases with configuration **UW** are higher than **WL**, even exceeding Betz limit [23], while those with **DW** are lower than **WL**. As noted in the previous work [7], this behavior is attributed to the bound-circulation systems of the lifting-devices. These bound-circulations accelerate the flow passing through the rotor part for configuration **UW**, whereas decelerate it for configuration **DW**. This effect is evident through observing the contours of $\overline{u}$ directly above the MRSLs shown in Figure 2.

5.2. Velocity fields

Figure 2 displays slices of time-averaged streamwise velocity $\overline{u}$ overlaid with arrows indicating the other velocity components ($\overline{v}$ and $\overline{w}$) for the cases subjected to $\mathrm{TI}_\infty = 5.37\%$. These contours highly resemble to those presented by Li *et al.* [7]. Unlike the cases with configuration

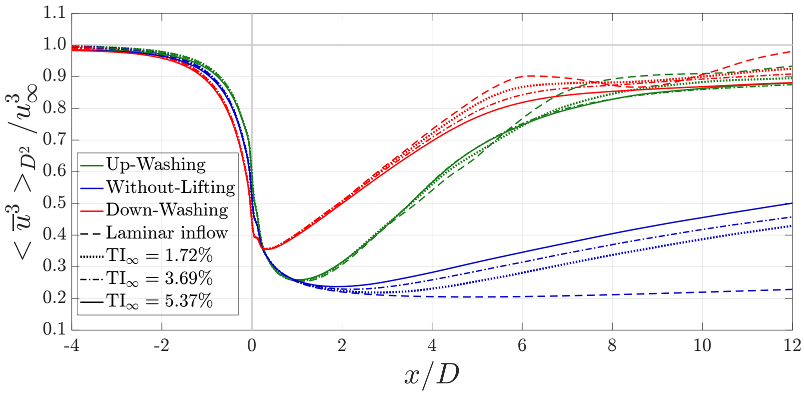

Figure 3. Area-averaged mean available power $< \overline{u}^3 >_{D^2}$ along the streamwise direction. The averaging area is the projection area of MRSL (see the black squares in Figure 2).

WL, the wakes behind the MRSLs of configurations **UW** and **DW** are diverted away from the MRSL's projection area. This indicates higher energy can be harvested if a downstream MRSL is positioned there. As reported in the previous work [7], **UW** channels the wake predominantly upward while **DW** directs the wake downward and then sideward. Additionally, by focusing on the x-plane contours, it can be seen that **WL** exhibits the largest wake deficit among the three, highlighting that both **UW** and **DW** recover their wakes faster compared to **WL**.

Although the contours of $\overline{u}$ show that both **UW** and **DW** achieve more pronounced wake recovery compared to **WL**, configuration **UW** appears to be superior. This is because the apparent wind farm layouts are influenced by wind direction, and the wake of **DW** may still hit the downstream MRSLs. In contrast, most of the wake of **UW** is lifted upward beyond the top height of MRSL, eliminating the possibility of hitting the downstream machines. However, these observations are preliminary, as wake-wake interactions among clustered MRSLs (i.e., RGWFs) can be highly complex. Dedicated studies on wake-wake interactions across various RGWF layouts are necessary to draw definitive conclusions regarding farm operations.

In addition to the time-averaged velocity fields, animations of the instantaneous velocity fields are available in the accompanying data repository [11]. These animations qualitatively reveal that the vortical structures corresponding to the released tip-vortices of **UW** and **DW** remain persistent in both magnitude and location under $\mathrm{TI}_\infty = 5.37\%$

5.3. Available power within the MRSL projection along the streamwise direction

Figure 3 presents the area-averaged mean available power, denoted as $< \overline{u}^3 >_{D^2}$, along the streamwsie direction. The area of interest is the region within the MRSL's projection. All cases in Table 1 are included. Comparing different MRSL configurations, both **UW** and **DW** exhibit significantly higher $< \overline{u}^3 >_{D^2}$ values compared to **WL** across all inflow conditions. Additionally, the slopes of $< \overline{u}^3 >_{D^2}$ for **UW** and **DW** are noticeably steeper than those for **WL**.

The curves of $< \overline{u}^3 >_{D^2}$ for configuration **WL** are significantly influenced by TI_∞. Transitioning from perfectly laminar (unrealistic in real world) to turbulent inflow conditions changes the slope of $< \overline{u}^3 >_{D^2}$ for **WL** from zero to positive, and the values of $< \overline{u}^3 >_{D^2}$ at a given x-position are higher for cases with higher TI_∞, aligning with the literature [20].

In contrast, the curves of $< \overline{u}^3 >_{D^2}$ for configurations **UW** and **DW** are largely insensitive to inflow turbulence intensity. The curves for cases with laminar inflow conditions are quantitatively similar to those with turbulent inflow conditions at $\mathrm{TI}_\infty = 5.37\%$, with ambient turbulence only slightly reducing the efficacy of the lifting-devices. These results provide strong evidence that the MRSL concept is robust against variations in ambient turbulence, namely, turbulence proof.

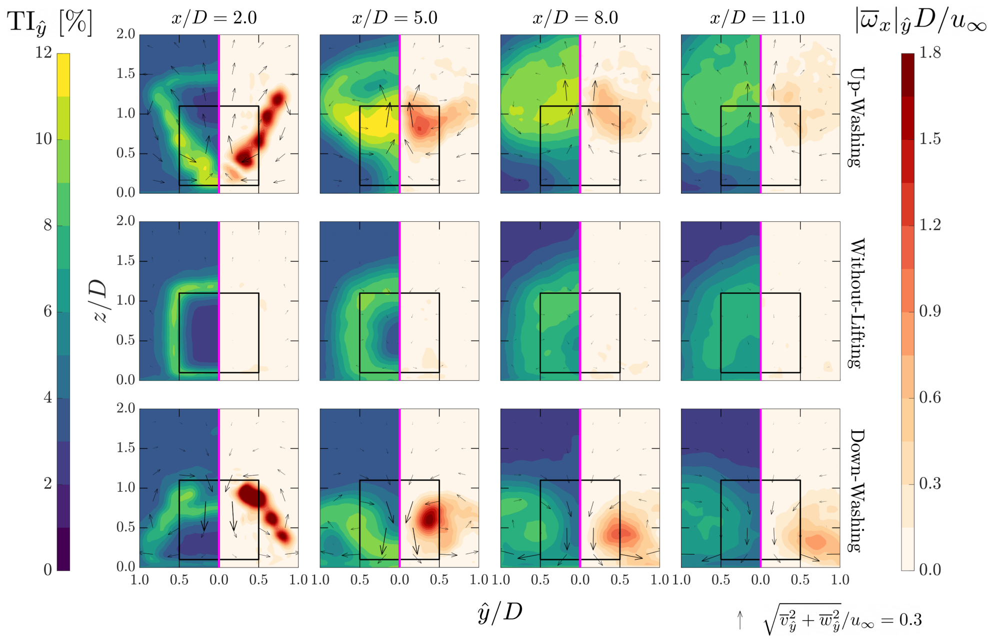

Figure 4. Contours of turbulence intensity (TI, left) and time-averaged streamwise vorticity ($\overline{\omega}_x$, right) at different x-planes for cases **UW-53** (top row), **WL-53** (middle row), and **DW-53** (bottom row). The x-planes are indicated at the top of each column. The subscript $\hat{y}$ denotes averaging over the symmetry plane $y/D = 0$ (see Equation 4). Arrows' are scaled by the square root of the in-plane velocity's norm with their absolute scales provided in the bottom right.

5.4. Contours of vorticity and turbulent kinetic energy

In addition to velocity, fields of time-averaged streamwise vorticity $\overline{\omega}_x$ and the turbulence intensity TI are examined. The focus on $\overline{\omega}_x$ arises from its close association with the released tip-vortices, which are responsible for inducing vertical flows. TI is considered because it governs key aspects of wind farm aerodynamics, including the convection of coherent structures, wake development, and the fatigue loads on the downstream machines [3]. Note that TI is linked with the turbulent kinetic energy $\overline{k} = 0.5\overline{u_i' u_i'}$ through $\mathrm{TI} = \sqrt{(2\overline{k}/3)}/u_\infty$.

In this work, the properties with subscript $\hat{y}$ indicate that they are averaged over the symmetry plane $y/D = 0$, as defined in Equation 4 ($\pm$ represents minus only when B is a y-component of a vector; otherwise, $\pm$ represents plus). Contours of $|\overline{\omega}_x|_{\hat{y}}$ and $\mathrm{TI}_{\hat{y}}$ at different x-planes for cases subjected to $\mathrm{TI}_\infty = 5.37\%$ are presented in Figure 4. In each panel, the right side displays the contours of $|\overline{\omega}_x|_{\hat{y}}$, while the left side shows the contours of $\mathrm{TI}_{\hat{y}}$.

$$\text{For property } B(x,y,z): \quad B_{\hat{y}}(x,\hat{y},z) = [B(x,y,z) \pm B(x,-y,z)]/2 \tag{4}$$

In Figure 4, the tip-vortices of the MRSL with configurations **UW** and **DW** are visible in the contours of $|\overline{\omega}_x|_{\hat{y}}$, especially at smaller x/D, where individual tip-vortices are distinctly outlined. As these vortices travel downstream, they merge and diffuse, and their mutual interactions become apparent. For configuration **UW**, the vortices are propelled upward and exhibit clockwise rotation on the $y/D > 0$ side. In contrast, configuration **DW** shows the opposite behavior. A notable difference between **UW** and **DW** is the influence of the ground, which causes a more pronounced sideward offset for the vortex system in **DW** compared to **UW** [7]. Although the maximum values of $|\overline{\omega}_x|_{\hat{y}}$ appear to be better maintained for **DW** than **UW**, indicating the vortical structures are better preserved and thus resulting in stronger induced

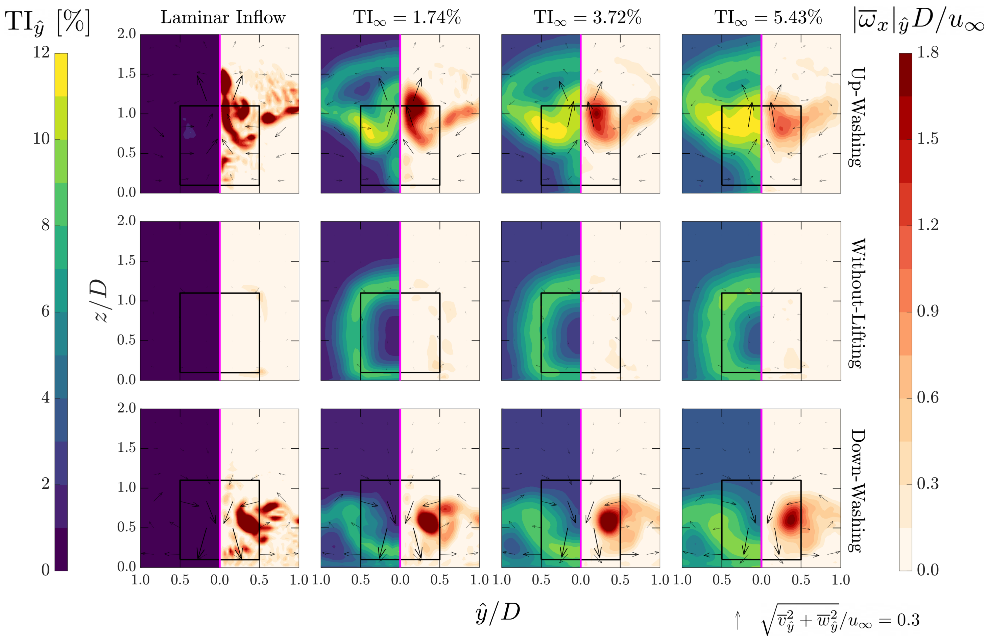

Figure 5. Contours of turbulence intensity (TI, left) and time-averaged streamwise vorticity ($\overline{\omega}_x$, right) at $x/D = 5$ for cases with different TI_∞, as indicated at the top of each column. The MRSL configurations shown in the top, middle, and bottom rows are **UW**, **WL**, and **DW**, respectively. The subscript $\hat{y}$ denotes averaging over the symmetry plane $y/D = 0$ (see Equation 4). Arrows's length are scaled by the square root of the in-plane velocity's norm.

flows, **UW** is considered more effective for vertical entrainment. This is because the vortex cores of **UW** are positioned closer to the MRSL's top, promoting stronger mixing between the wake and the upper-layer freestream. However, as stated earlier, whether **UW** is better than **DW** in the context of overall wind farm power output should be further studied.

Focusing on the contours of $\mathrm{TI}_{\hat{y}}$ in Figure 4, it can be seen that the high values concentrated around the edge of the wake or the vicinity of the tip-vortices. Notably, higher values of $\mathrm{TI}_{\hat{y}}$ correlate with stronger mixing and entrainment. For **UW**, the high $\mathrm{TI}_{\hat{y}}$ region extends beyond $z/D = 2$ as $x/D > 5$, indicating significant interaction between the wake and the upper freestream layer. On the other hand, **DW** exhibits blobs of high $\mathrm{TI}_{\hat{y}}$ at $\hat{y} > 0.5$, showing the entrainment of flow energy occurs mainly from the sides. For **WL**, the high $\mathrm{TI}_{\hat{y}}$ regions are largely confined to the edges of the MRSL's projection, indicating mixing is limited in those layers. Interestingly, while **UW** shows higher TI levels compared to **WL**, **DW** exhibits similar or even lower TI levels than **WL** beyond $x/D = 8$. This suggests that the lifting-devices can elevate available power without increasing the fatigue loads of the downstream machines. This aspect is critical for real-world application, as faster wake recovery is typically associated with higher turbulence levels [24], adversely impacting the fatigue loads on downstream turbines.

Figure 5 displays the contours of $|\overline{\omega}_x|_{\hat{y}}$ and $\mathrm{TI}_{\hat{y}}$ measured at $x/D = 5$ for all cases in Table 1, where the impacts of TI_∞ are evaluated. Not surprisingly, tip-vortices merge and diffuse more rapidly with higher TI_∞, as ambient turbulence disrupts the coherent structures in wind turbine wakes [20]. However, it is worth recalling that $< \overline{u}^3 >_{D^2}$ along the streamwise direction is not profoundly affected by TI_∞ as shown in Figure 3, showing that the concept of MRSL remains effective under higher TI_∞, even though the coherent structures are less maintained. Regarding $\mathrm{TI}_{\hat{y}}$, Figure 5 shows cases with higher TI_∞ have higher turbulence levels, while the shapes of the contours are very similar for the cases subjected to turbulent inflow conditions.

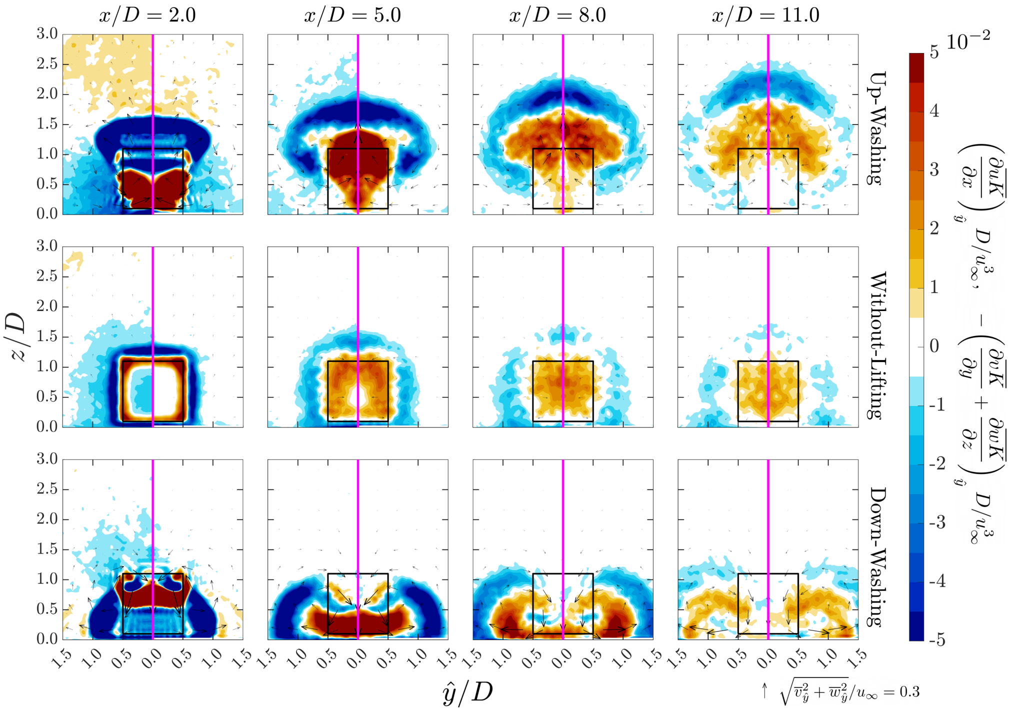

Figure 6. Contours of the energy equation's terms (Equation 5) for cases **UW-53** (top row), **WL-53** (middle row), and **DW-53** (bottom row). The left of each panel plots the contour of $\partial\overline{uK}/\partial x$. The right plots the contours of $-(\partial\overline{vK}/\partial y + \partial\overline{wK}/\partial z)$. The x-planes are indicated at the top of each column. Arrows are scaled by the square root of the in-plane velocity's norm.

5.5. Redistribution of the flow energy in the wake

This part further examines the wake recovery process in terms of the time-averaged energy equation for incompressible flow, shown in the left of Equation 5, where K denotes the instantaneous kinetic energy ($K = 0.5u_iu_i$). By grouping the contributions of pressure gradients ($\partial p/\partial x_i$), viscosity (ν), and SGS effects (ν_{SGS}) to a residual term $\mathcal{R}$, the energy equation is simplified to the right of Equation 5. This simplified form governs the redistribution of the kinetic energy flux rate, with $\mathcal{R}$ accounting for residual. This analysis focuses on term $\partial\overline{uK}/\partial x$, as wake recovery is directly associated with its sign and magnitude.

$$\frac{\partial\overline{u_iK}}{\partial x_i} = -\frac{1}{\rho}\frac{\partial\overline{u_ip}}{\partial x_i} + \overline{u_i\frac{\partial}{\partial x_j}\left[(\nu+\nu_{\mathrm{SGS}})\frac{\partial u_i}{\partial x_j}\right]} \quad\longrightarrow\quad \frac{\partial\overline{uK}}{\partial x} = \left[-\left(\frac{\partial\overline{vK}}{\partial y}+\frac{\partial\overline{wK}}{\partial z}\right)\right] + \mathcal{R} \qquad (5)$$

Figure 6 illustrates the terms of the energy equation in Equation 5 for the cases with $\mathrm{TI}_\infty = 5.37\%$. The left of each panel shows $\partial\overline{uK}/\partial x$, while the right displays $-(\partial\overline{vK}/\partial y + \partial\overline{wK}/\partial z)$. A comparison between the left and right of each panel reveals that the contribution of $\mathcal{R}$ is minimal, indicating the terms related to $\partial p/\partial x_i$, ν, and ν_{SGS} may be omitted.

In the middle row of Figure 6, the energy redistribution for **WL** is predominantly confined near the edges of the projection of the MRSL. In contrast, the flow energy for wake recovery of **UW** is primarily driven by potent vertical entrainment from the region directly above the MRSL, with the energy exchange penetrating up to $z/D = 2.5$ at $x/D = 11$, and the magnitude of energy redistribution for **UW** is significantly greater than for **WL**. Regarding **DW**, the energy exchange between the wake and the freestream occurs mainly along the sides and is restricted below $z/D = 1.2$, suggesting a weaker vertical entrainment compared to **UW**. Instead, **DW** recovers the wake by depleting the flow energy from the sides. This diminishes the incoming

Journal of Physics: Conference Series **3016** (2025) 012042 doi:10.1088/1742-6596/3016/1/012042

flow energy for the downstream machines if the wind farm layout were staggered, resulting in lowering their power output. However, further research is needed to determine the optimal configuration of MRSL for RGWF in terms of overall wind farm power output.

6. Conclusion

This study investigated the wake aerodynamics of multi-rotor systems with lifting-devices (MRSL) using large-eddy simulation with actuator techniques under the conditions that wind shear is absent. The findings confirm that both configurations **Up-Washing** and **Down-Washing** achieve significantly faster wake recovery compared to the machine without lifting-devices (**Without-Lifting**). Also, it is demonstrated that changes in the ambient turbulence level have minimal impact on the increased wake recovery rate, highlighting the robustness and effectiveness of MRSL as a promising new technology/concept for future wind energy.

Configuration **Up-Washing** is currently postulated to be superior in terms of vertical entrainment, as its vortex systems more effectively promote interaction between the wake in lower layers and the freestream in uppers layer. On the other hand, configuration **Down-Washing** shows the capability of enhancing wake recovery while maintaining or even reducing the wake turbulence levels, which is advantageous for the downstream machines' fatigue loads.

Future research regarding exploring wake-wake interactions within the clustered MRSLs (i.e., regenerative wind farms, RGWFs) and assessing their performance when subjected to realistic atmospheric boundary layers are recommended. Also, experimental validation of the current findings are essential to advance MRSL technology from concept to practical application.

References

[1] Ritchie H 2022 How does the land use of different electricity sources compare? `https://ourworldindata.org/land-use-per-energy-source` Accessed on 2nd Jan. 2025
[2] BloombergNEF 2024 New energy outlook 2024 `https://about.bnef.com/new-energy-outlook/` Accessed on 2nd Jan. 2025
[3] Stevens R J and Meneveau C 2017 *Annual review of fluid mechanics* **49** 311–339
[4] Ferreira C, Bensason D, Broertjes T J, Sciacchitano A *et al.* 2024 *Journal of Physics: Conference Series* vol 2767 (IOP Publishing) p 092107
[5] Broertjes T, Bensason D, Sciacchitano A and Ferreira C 2024 *Journal of Physics: Conference Series* vol 2767 (IOP Publishing) p 072012
[6] Avila Correia Martins F, van Zuijlen A and Simão Ferreira C 2025 *Wind Energy Science* **10** 41–58
[7] Li Y, Yu W, Sciacchitano A and Ferreira C 2025 *Wind Energy Science* **10** 631–659
[8] United Nations 2016 *Treaty Series* **3156** 79
[9] McKinsey&Company 2024 Global energy perspective 2024 `https://www.mckinsey.com/industries/energy-and-materials/our-insights/global-energy-perspective#/` Accessed on 27th Dec. 2024
[10] Wind Europe 2024 Wind energy in europe: 2023 statistics and the outlook for 2024-2030 `https://windeurope.org/intelligence-platform/` Accessed on 2nd Jan. 2025
[11] Li Y, Yu W, Sciacchitano A and Ferreira C 2025 Supplementary animations and simulation settings for "Wake aerodynamic of multi-rotor system with lifting-devices under different ambient turbulence" `https://doi.org/10.4121/5f7a7582-d1a4-4ed6-af00-7f0bfbc274e6` 4TU.ResearchData
[12] Selig M S, Guglielmo J J, Broeren A P and Giguere P 1995 *Summary of Low-Speed Airfoil Data: Volume 1*
[13] Sorensen J N and Shen W Z 2002 *J. Fluids Eng.* **124** 393–399
[14] Mikkelsen R F 2004 Ph.D. thesis Technical University of Denmark
[15] Gao Z, Li Y, Wang T, Ke S and Li D 2021 *Applied Mathematics and Mechanics* **42** 511–526
[16] Martínez-Tossas L A, Churchfield M J and Leonardi S 2015 *Wind Energy* **18** 1047–1060
[17] OpenCFD Ltd 2023 `https://www.openfoam.com` Accessed on 27th Dec. 2024
[18] Meneveau C, Lund T S and Cabot W H 1996 *Journal of fluid mechanics* **319** 353–385
[19] Poletto R, Craft T and Revell A 2013 *Flow, turbulence and combustion* **91** 519–539
[20] Li Y, Yu W and Sarlak H 2024 *Wind Energy* **27** 1499–1525
[21] Li Y, Yu W and Sarlak H 2025 *Renewable Energy* **239** 122062
[22] Hansen K S, Barthelmie R J, Jensen L E and Sommer A 2012 *Wind Energy* **15** 183–196
[23] Manwell J F, McGowan J G and Rogers A L 2010 (John Wiley & Sons)
[24] VerHulst C and Meneveau C 2015 *Energies* **8** 370–386